Reconfiguring Hierarchical Porous Architecture of 2D Metal Nanosheets for Multifunctional Triboelectric Nanogenerators

Dae-Hong Kim, Ju-Hyoung Yu, Cheoljae Lee, Min-Young Seo, Seungyeon Kim, Hyeonji Joo, Young-Seok Song, Sukang Bae, Ju-Hyuck Lee, Seoung-Ki Lee, and Tae-Wook Kim**

2D single-crystalline metal nanosheets are a promising platform for self-powered electronics, yet their potential for triboelectric nanogenerators (TENGs) remains unexplored. A key challenge in TENGs is overcoming low current output and limited durability. A hierarchical porous copper nanosheet-based TENG (HPC-TENG) is reported to substantially enhance triboelectric performance through a unique structural design. The method uses a simple spray-coating process to create a hierarchical porous conductive film from 2D copper nanosheets (Cu NSs). By infiltrating this film with polydimethylsiloxane (PDMS), interfacial contact is maximized, significantly boosting charge generation during mechanical cycling. The HPC-TENG achieves a remarkable 590% enhancement in electrical output compared to conventional Cu thin-film TENGs, while maintaining stable operation over 100 000 cycles. Beyond energy harvesting, this architecture provides integrated multifunctionality, including stable electromagnetic interference (EMI) shielding effectiveness exceeding 30 dB and efficient Joule heating. These findings highlight the strong potential of hierarchical porous metal nanosheet electrodes as a versatile platform for advanced energy harvesting, EMI shielding, and flexible heating, opening new avenues for next-generation wearable electronics.

1. Introduction

Since the invention of silicon based electronic components, such as the widely used silicon transistor in the 20th century, significant attention has been directed toward the development of advanced electronic devices with reduced size, enhanced functionality, and lower power consumption.[1,2] At the same time, considerable efforts have been made to establish new device platforms that offer freedom in shape, dimensions, and function.[3–5] In response to these demands, wearable and flexible electronics have emerged as a promising class of technologies, providing lightweight form factors, mechanical robustness, and the ability to conform to and interact naturally with the surrounding environment.[6–8] However, delivering a continuous and reliable power supply to such advanced electronics remains a major challenge. Traditional power sources, such as wired

---

D.-H. Kim, M.-Y. Seo, S. Kim, H. Joo, Y.-S. Song, T.-W. Kim
Department of Flexible and Printable Electronics
LANL-JBNU Engineering Institute-Korea
Jeonbuk National University
Jeonju 54896, Republic of Korea
E-mail: twk@jbnu.ac.kr

J.-H. Yu, S.-K. Lee
School of Materials Science and Engineering
Pusan National University
2, Busandaehak-ro-63-beon-gil, Busan, Geumjeong-gu 46241, Republic of Korea
E-mail: ifriend@pusan.ac.kr

The ORCID identification number(s) for the author(s) of this article can be found under https://doi.org/10.1002/adma.202515466

DOI: 10.1002/adma.202515466

C. Lee, J.-H. Lee
Department of Energy Science and Engineering
Daegu Gyeongbuk Institute of Science & Technology (DGIST)
Daegu 42988, Republic of Korea

S. Bae
Functional Composite Materials Research Center
Institute of Advanced Composite Materials
Korea Institute of Science and Technology
Jeollabuk-do 55324, Republic of Korea

S.-K. Lee
Institute of Materials Technology
Pusan National University
2, Busandaehak-ro-63-beon-gil, Busan, Geumjeong-gu 46241, Republic of Korea

T.-W. Kim
Department of JBNU-KIST Industry-Academia Convergence Research
Jeonbuk National University
567 Baekje-daero, Jeonju, Deokjin-gu 54896, Republic of Korea

connections and batteries, are often unsuitable for portable and flexible systems due to their bulkiness and limited integration compatibility.[9–11] As a result, energy harvesting has emerged as a compelling approach for powering next generation electronics by converting ambient energy sources into usable electricity. This self-sustaining strategy eliminates the need for external power by harnessing stimuli such as solar radiation, airflow, water motion, and human activities.[12–14] Among various energy harvesting technologies, triboelectric nanogenerators (TENGs) have gained increasing attention due to their structural simplicity, mechanical flexibility, low cost, and ability to convert a wide range of mechanical forces into electrical energy.[15]

TENGs convert mechanical energy into electrical energy through the coupled mechanisms of contact electrification and electrostatic induction.[16,17] When two materials with differing electron affinities come into contact and separate repeatedly, surface charges are generated through electron transfer. The movement of these charges under an induced electric field results in a potential difference across the electrodes, thereby producing current flow. Depending on the configuration of the electrodes and the method of charge collection, triboelectric nanogenerators are generally classified into two operational modes: dual electrode and single electrode configurations.[18]

The dual electrode mode, one of the most widely adopted, employs two electrodes attached to triboelectric surfaces. Relative motion between the friction layers generates charge induction and current flow between the electrodes. Although this setup provides high output performance due to contributions from both electrodes to dynamic capacitance variation, it requires additional wiring and electrode components, which increases structural complexity and reduces suitability for flexible or wearable devices. As a more practical alternative, the single electrode mode has been introduced as a simpler and more adaptable configuration. In this design, only one electrode is connected to the external circuit, while the counter surface is grounded or left floating.[17,19] This configuration reduces device weight, enhances mechanical compliance, and enables conformal integration with arbitrarily shaped surfaces such as human skin or textiles. Owing to these advantages, single electrode systems are especially attractive for applications in wearable electronics, human machine interfaces, and self-powered biomedical systems.[20–23] Despite their practical benefits, single electrode devices typically show lower output performance than dual electrode systems due to limited dynamic capacitance modulation, as only one electrode participates in charge induction.[17]

To address this critical performance limitation in single-electrode TENGs, many studies have focused on enhancing their output through various material and structural engineering strategies. A widely investigated approach involves introducing micro or nanostructures onto the friction layer, which increases the effective contact area and enhances surface charge density.[24,25] However, surface-engineered structures often suffer from mechanical degradation under repeated use, resulting in limited long-term stability.[15,26] As an alternative, integrating fillers into a dielectric layer serving as a matrix has emerged as a promising approach for enhancing the electrical output of TENGs. First, numerous studies have reported the use of metal–organic frameworks (MOFs) as fillers to improve TENG performance.[27–30] The incorporation of MOFs can enhance the charge storage capability of the friction layer, thereby significantly improving device performance. In addition, embedding conductive nanomaterials such as 0D nanoparticles, 1D nanowires, and carbon nanotubes (CNTs), and 2D materials (e.g., MXene, graphene, MoS_2) into the dielectric layer has been actively investigated.[31–39] These conductive materials enhance the dielectric capacitance either by increasing the dielectric constant of the matrix or by inducing more charges through their large specific surface area. In particular, the incorporation of aligned conductive materials within the dielectric further improves the dielectric capacitance.[36,37,40,41] Among these conductive nanomaterials, 2D layered materials have been considered as especially promising fillers for TENG and sensor applications due to their large surface area, excellent conductivity, and tunable surface properties, which effectively enhance charge storage capacity and dielectric performance.[42]

In addition, innovative electrode designs, such as the use of serrated aluminum wool, have been shown to increase the interfacial area with the dielectric and improve charge collection.[43] Nevertheless, many of these approaches rely on multi material systems beyond the core dielectric and electrode layers and often require complex and multi-step fabrication processes. Moreover, most prior studies have primarily focused solely on maximizing electrical output, often overlooking the critical practical requirements of wearable and flexible electronics, including material simplicity, scalable fabrication, and the integration of diverse functionalities. These limitations highlight that, for triboelectric nanogenerators to move beyond proof-of-concept demonstrations and achieve true integration into wearable and portable electronics, multifunctionality is indispensable. From a functional standpoint, one of the most critical requirements is the ability to protect sensitive electronic components from surrounding electromagnetic noise, which can otherwise compromise stable operation and reliable signal transmission.[44,45] At the same time, effective electromagnetic shielding mitigates the adverse impact of electromagnetic waves on the human body, thereby ensuring safety when such devices are worn in direct contact with the skin.[46] Importantly, a next-generation wearable and portable TENG should therefore incorporate electromagnetic shielding capabilities not only to safeguard device performance but also to broaden the spectrum of practical applications.[47] In addition, Joule heating functions are equally valuable, providing on-demand thermal management and enhanced user comfort for body-mounted devices. These considerations emphasize that future TENG platforms must be designed not only for high energy-harvesting efficiency but also for integrated multifunctionality, which is essential to meet the real demands of wearable and flexible electronic systems.

Herein, we present an unprecedented, structurally engineered single electrode triboelectric nanogenerator (HPC-TENG) that decisively addresses longstanding limitations in performance, fabrication complexity, and multifunctionality. Our approach leverages solution-processable 2D single crystalline copper nanosheets (Cu NSs), which spontaneously assemble into a highly interconnected hierarchical porous film with intrinsically aligned nanosheets forming abundant internal voids, eliminating the need for complex multi-step patterning or additional conductive fillers. By infiltrating this unique electrode structure with a single dielectric material (PDMS), the resulting device

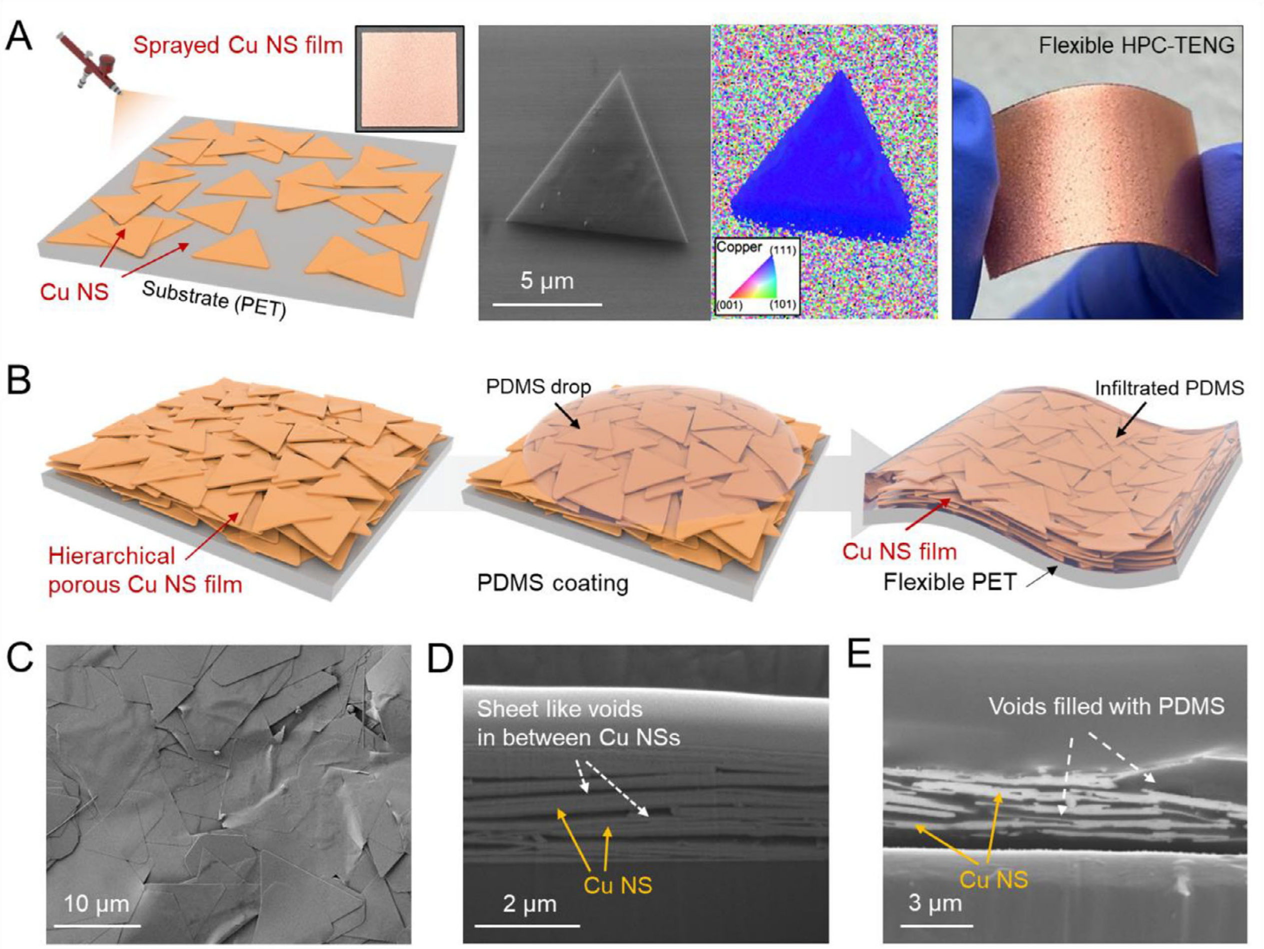

Figure 1. Fabrication process and structural features of the hierarchical porous copper nanosheet-based triboelectric nanogenerator (HPC-TENG). A) Schematic illustration of the spray coating process to form a copper nanosheet (Cu NS) film on a PET substrate. (left) SEM and EBSD images confirm the single-crystalline structure of a triangular Cu NS. (middle) Photograph of the flexibility of the fabricated HPC-TENG. (right) B) Sequential schematic diagrams showing the hierarchical porous structure formation of the Cu NS film and subsequent PDMS spin-coating and curing to yield a flexible HPC-TENG device. C) Top-view SEM image of the Cu NS film, exhibiting a disordered yet interconnected network. D) Cross-sectional SEM image of the Cu NS film, highlighting the formation of hierarchical sheet-like voids between stacked nanosheets. E) Cross-sectional SEM image after PDMS infiltration, showing the voids effectively filled by the dielectric material.

demonstrates remarkable performance enhancement purely through internal structural engineering, fundamentally simplifying the material composition and fabrication process. This innovative configuration enables scalable production, robust long-term stability, and integrated multifunctionalities, including sustained electromagnetic interference (EMI) shielding effectiveness exceeding 30 dB even after prolonged cycling, and highly efficient, tunable Joule heating, achieving steady-state temperatures up to 59.4°C at 5 V. We believe that our findings offer a streamlined design paradigm for high-performance triboelectric energy harvesters and highlight transformative possibilities for multifunctional wearable electronics and integrated self-powered systems.

2. Results and Discussion

The fabrication and structural characteristics of the hierarchical porous copper nanosheet film based triboelectric nanogenerator (HPC-TENG) are schematically illustrated in **Figure** 1A,B. The device was fabricated through a straightforward two step solution process involving spray coating and spin coating. As shown in Figure 1A, a copper nanosheet (Cu NS) film was formed on a PET substrate via spray coating. The SEM and EBSD images reveal that the triangular Cu NSs are single crystalline with a predominant (111) orientation (also confirmed in Figure S1, Supporting Information), which ensures high electrical conductivity. The flexibility of the fabricated HPC-TENG is also demonstrated in the photograph. Figure 1B presents sequential schematic diagrams of the fabrication process, including the formation of a hierarchical porous Cu NS film, followed by PDMS spin coating and thermal curing to complete the flexible HPC-TENG device. It comprises a PET substrate, a Cu NS film functioning as the single electrode, and a PDMS layer serving as the dielectric component. The HPC-TENG operates in the single electrode mode, which is one of the four working mechanisms of triboelectric nanogenerators.[17] The Cu NSs, which constitute the building blocks of the electrode, were synthesized and purified using a conventional hydrothermal method. These 2D nanosheets exhibit lateral sizes of several micrometers and thicknesses of tens of nanometers. They are single crystalline with a predominant (111) orientation, which imparts high electrical conductivity.[48] The Cu NSs were dispersed in chloroform and deposited by spray coating onto the PET substrate to form the Cu NS film (Figure 1C). Due to their high aspect ratio, the nanosheets spontaneously aligned parallel to the substrate during deposition, resulting in a horizontally oriented network containing vertically distributed voids, thus forming a hierarchical porous structure. To further substantiate these structural characteristics, we quantitatively analyzed the porosity of the Cu NS film. The Cu NS film is composed of ≈25%–34% Cu NSs, corresponding to a reported porosity of 75%–66%.[49] Cross-sectional SEM imaging (Figure 1D) reveals the internal sheet-like voids and interconnected network, which contribute simultaneously to high porosity and in-plane electrical conductivity. Furthermore, nondestructive 3D X-ray microscopy (XRM) analysis (Figure S2 and Video S1, Supporting Information) confirmed an internal porosity of ≈65%, consistent with previous literature values and quantitatively validating the hierarchical porous architecture of the Cu NS film.

In single electrode TENGs, the electrode plays a vital role in collecting and transferring triboelectric charges to the external circuit with minimal loss.[18] The high conductivity and large surface area of the Cu NS film are expected to facilitate efficient charge transport, thereby enhancing the overall electrical output. Following electrode fabrication, a PDMS layer was spin coated onto the Cu NS film. During this step, the PDMS naturally infiltrated the internal voids of the Cu NS network, forming a solution infiltrated composite structure as shown in Figure 1E. The unique porous morphology of the Cu NS film not only enabled effective PDMS infiltration but also provided a means to modulate the interfacial area between the dielectric and electrode layers. Importantly, the thickness of the PDMS infiltrated layer can be tuned by controlling the initial thickness of the Cu NS film during the spray coating step. This spontaneous formation of a vertically heterogeneous, yet planar, conductive network offers a distinct advantage over previously reported strategies to enhance TENG output. Prior studies have shown that introducing 2D conductive materials, such as MXene or horizontally aligned graphene sheets, into dielectric matrices can improve device performance.[36,37] However, these methods typically require additional materials beyond the electrode and dielectric, as well as extra alignment processes to control the orientation of the conductive fillers. In contrast, the HPC-TENG developed in this study relies solely on a single dielectric and a single electrode material, while taking advantage of the natural alignment behavior of Cu NSs during spray coating. This approach offers clear benefits in terms of structural simplicity, process scalability, and fabrication efficiency.

To investigate the formation and modulation of the internal structure in the HPC-TENG, we systematically varied the loading weight of the Cu NSs, defined as the mass per unit area in mg cm^{-2}, at five different levels: 0.25, 0.5, 1.0, 2.0, and 4.0 mg cm^{-2}. In our previous study, we demonstrated that the hierarchical porous structure of Cu NS films evolves with increasing loading weight.[49] To validate this structural evolution within the actual HPC-TENG device, three representative loading weights (0.5, 1.0, and 2.0 mg cm^{-2}) were selected for detailed structural characterization using schematic illustrations and cross-sectional SEM images, as shown in **Figure 2**. As the loading weight increased, the Cu NS film became progressively thicker, and its hierarchical porous morphology became more pronounced. This enhancement in structural porosity facilitated greater PDMS infiltration during spin coating, resulting in an increased interfacial area between the Cu NS network and the dielectric layer. Elemental mapping of Cu via energy dispersive X-ray spectroscopy (EDS) analysis (Figure 2G–I) further confirmed the spatial distribution of Cu NSs within the film, indicating that the degree of infiltration and internal architecture of the HPC-TENG can be effectively tuned by controlling the loading weight. Additional SEM and corresponding elemental mapping images, including both copper and silicon signals, for all loading weights (0.25, 0.5, 1.0, 2.0, and 4.0 mg cm^{-2}) are provided in Figure S3 (Supporting Information). Notably, the silicon mapping results clearly demonstrate that the internal voids of the Cu NS films were fully filled with PDMS across all tested loading conditions, validating the reliability of the solution infiltration process. Moreover, the electrical properties of the Cu NS films were assessed by measuring the sheet resistance at different loading weights. As summarized in Table S1 (Supporting Information), the sheet resistance decreased with increasing Cu NS content. Although the measured sheet resistance values were higher than those of conventional sputtered Cu films on PET, the resistance remained sufficiently low to ensure effective charge transport due to the high conductivity of the individual Cu nanosheets, even though the films were fabricated solely through spray coating without any additional thermal annealing. According to a previous study, the electrode–triboelectric material interface, surface roughness, and work function differences play a more significant role in determining TENG performance than electrode conductivity.[50] Therefore, the differences in conductivity among the films or the (111) crystallographic facet of Cu nanosheets are expected to have a relatively smaller impact on the TENG output compared to the differences caused by changes in the internal structure.

To evaluate the electrical output performance of the HPC-TENG, the Cu NS film electrode was electrically connected to external circuitry using silver paste. The open circuit voltage and short circuit current were measured using a digital oscilloscope and a precision electrometer, respectively. Electrical connections were configured such that the signal input of each device was connected to the HPC-TENG, and the reference was grounded. To ensure consistent mechanical input during electrical measurements, an electromagnetic shaker equipped with a stainless-steel (SS) cylinder was employed to drive the vertical contact and separation motion of the HPC-TENG. The stainless-steel cylinder acted as a positive triboelectric material when in contact with the HPC-TENG, and together with the 2 cm × 2 cm device formed an effective contact area of 1.767 cm^2, as illustrated in Figure S4C (Supporting Information). The applied pressure and frequency were maintained at 4.99 kPa and 5 Hz, respectively. Under these conditions, the two materials generated electrical signals through periodic vertical contact and release cycles, as schematically illustrated in Figure S4A (Supporting Information). The corresponding electrical output

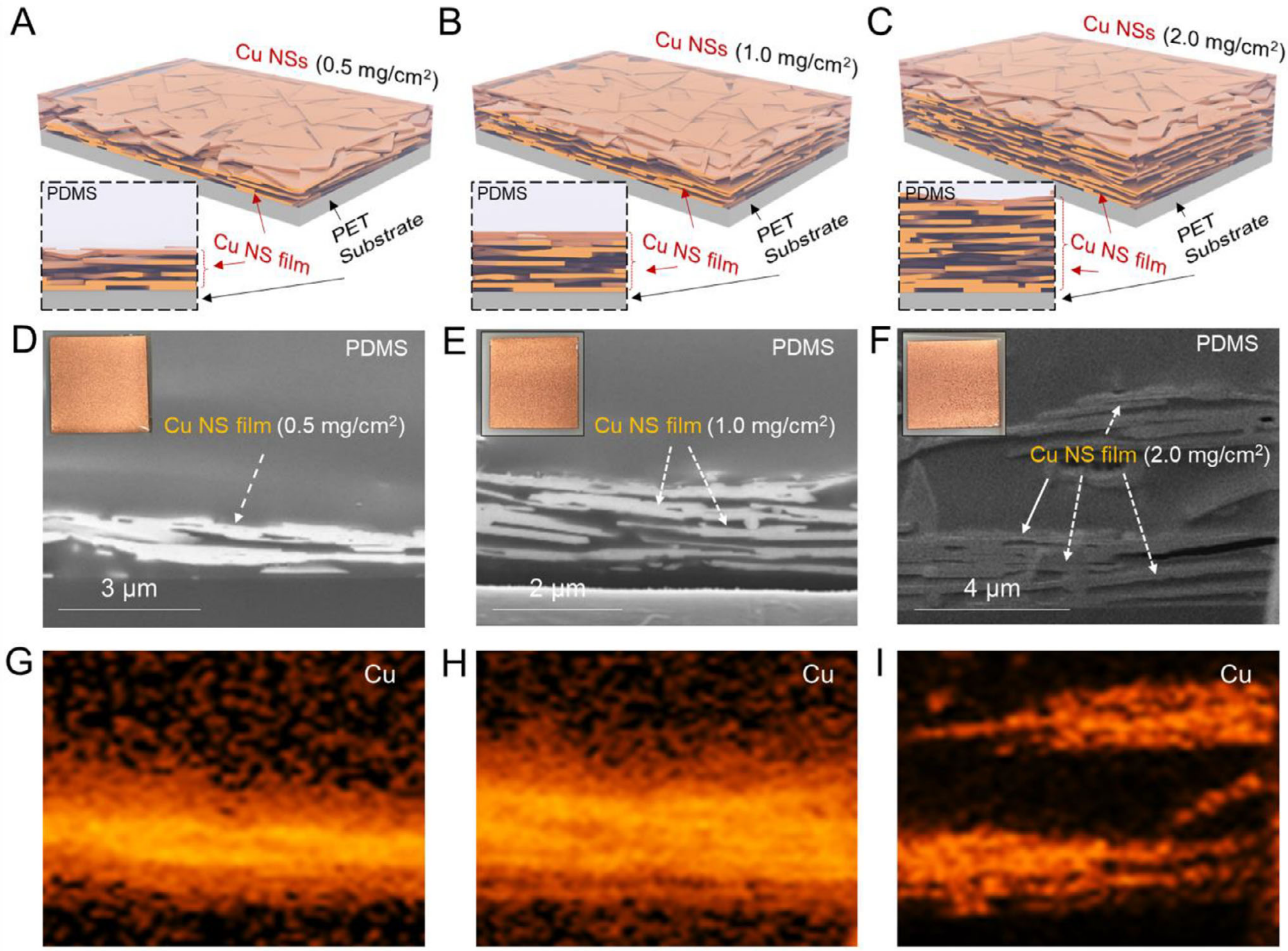

Figure 2. Structural modulation of HPC-TENGs as a function of Cu nanosheet loading weight. Schematic illustrations of hierarchical porous Cu nanosheet (Cu NS) films in HPC-TENGs with loading weights of A) 0.5 mg cm^{-2}, B) 1.0 mg cm^{-2}, and C) 2.0 mg cm^{-2}, showing increased stacking density and vertical layering of nanosheets. D–F) Corresponding cross-sectional SEM images of the Cu NS–PDMS composites with increased nanosheet stacking and thickness at higher loading weights. Insets: photographic images of the Cu NS films. G–I) EDS elemental mapping of copper in the same samples, confirming the vertical distribution and uniform dispersion of the Cu NSs within the dielectric matrix.

behavior of the HPC-TENG is presented in Figure S4B (Supporting Information), where the voltage signal exhibits a characteristic waveform reflecting the sequential stages of the contact–separation process. At the initial separation (Stage 1), no significant potential is observed due to the absence of interaction between the two surfaces. The stainless-steel electrode nears and makes contact with the PDMS surface (Stage 2), leading to a rapid increase in surface charge separation and resulting in a sharp positive voltage peak. As the contact is maintained, the potential stabilizes near zero due to the equilibrium state between the triboelectric layers. When the two surfaces are released (Stage 3), a sudden separation induces the movement of charges in the opposite direction, generating a negative voltage peak. This full cycle demonstrates the typical contact electrification and electrostatic induction process of a single electrode triboelectric nanogenerator, confirming the reliable and repeatable energy harvesting behavior of the HPC-TENG under vertical contact–separation mode. To assess the contribution of the Cu NS structure to device performance, a reference TENG was also fabricated using a conventional Cu thin-film. The film was deposited on a PET substrate via thermal evaporation, and a PDMS layer was subsequently applied to serve as the dielectric. This thin-film based TENG served as a control to directly compare the output characteristics with those of the HPC-TENG.

The electrical performance of the HPC-TENG was systematically evaluated under various structural and operational conditions, as shown in **Figure 3**. For the HPC-TENG, both the output voltage and current increased with the Cu NS loading weight, reached a maximum, and then gradually decreased (Figure 3A,B). To further provide a quantitative comparison of device performance, the charge density per cycle was calculated by integrating the current density over time from the data in Figure 3B,[51] and the corresponding results are presented in Figure S5 (Supporting Information). The maximum output was observed at a loading weight of 1.0 mg cm^{-2}, where the output voltage and current density were enhanced by factors of 1.97 and 3.01, respectively, compared to the Cu thin-film based TENG.

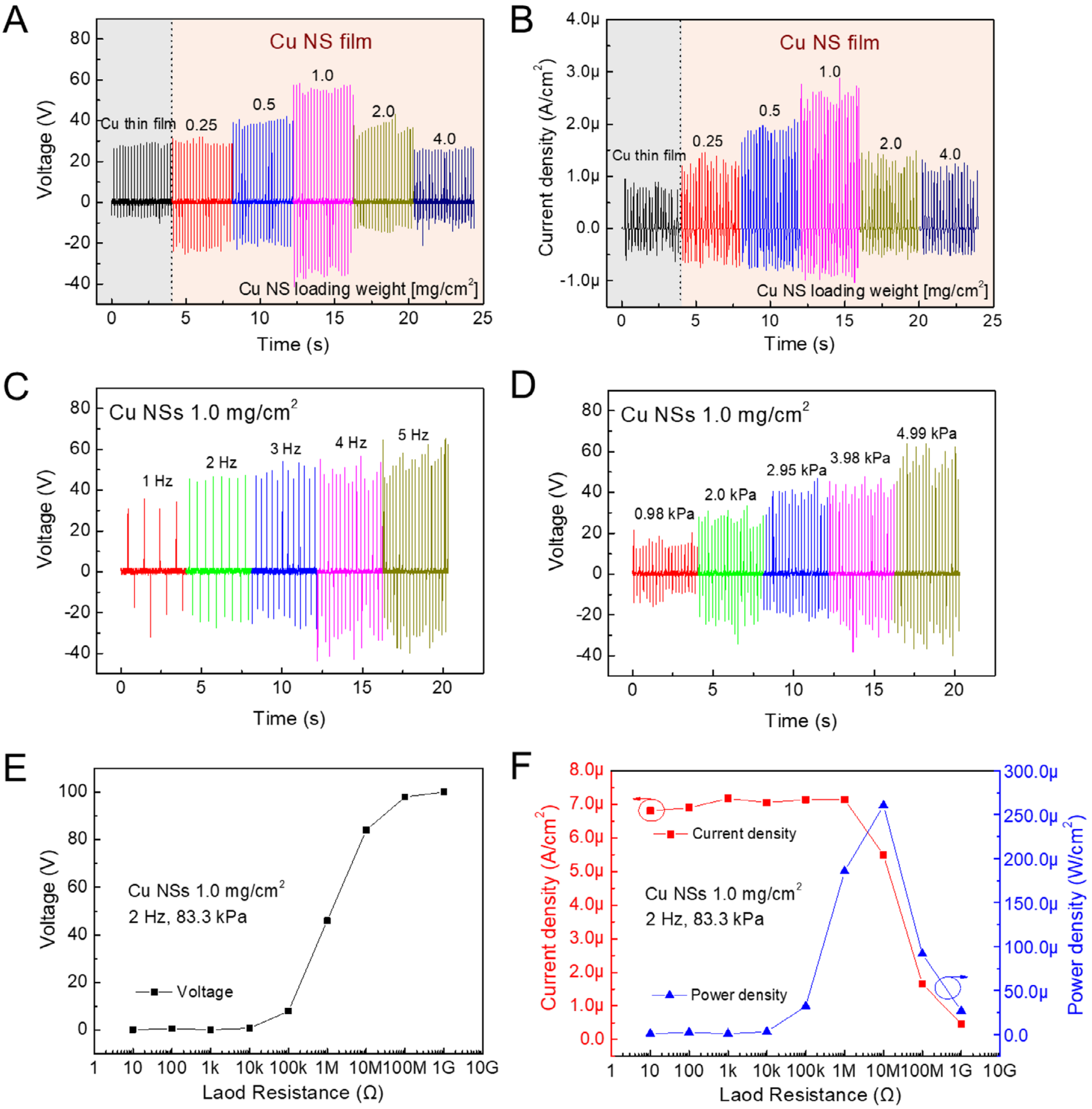

Figure 3. Electrical performance and operational stability of the HPC-TENG under varying conditions. A) Output voltage and B) current density of the HPC-TENG at different Cu nanosheet (Cu NS) loading weights ranging from 0.25 to 4.0 mg cm^{-2}, compared to a conventional Cu thin-film electrode. C) Output voltage at different vibration frequencies (1–5 Hz) for a fixed Cu NS loading weight of 1.0 mg cm-^{2}. D) Output voltage at various applied pressures (0.98–4.99 kPa) under 1.0 mg cm-^{2} Cu NS loading. E) Output voltage, F) current density, and calculated power density as a function of external load resistance under 2 Hz and 83.3 kPa, indicating optimal power transfer at 10 MΩ.

Consequently, the power density increased from 28.42 μW cm^{-2} for the Cu thin-film TENG to 168.19 μW cm^{-2}, representing an enhancement of ≈590% when normalized by the effective contact area. As shown in Figure 3, while the positive output of the Cu thin-film TENG and the HPC-TENG at a Cu NS loading of 0.25 mg cm^{-2} are comparable, a significant difference is observed in the negative output. This asymmetric behavior has been reported as a characteristic of contact–separation mode TENGs, where the voltage in the contact state is determined primarily by the dielectric thickness, while the voltage in the separation state is influenced by the separation distance.[52] In the HPC-TENG, the hierarchical porous structure of the Cu NS film provides a broader and more stable electrode–dielectric interface, enabling more effective charge separation during the separation process and resulting in a much higher negative output peak compared to the Cu thin-film TENG.

To further examine the influence of the triboelectric pairing, the counter material of the HPC-TENG was replaced with aluminum foil, and copper foil, and the corresponding output performance was evaluated (See Figure S6, Supporting Information). Aluminum and copper are metallic materials generally classified as more tribopositive than PDMS in the triboelectric series.[53] Similar to the results obtained with stainless-steel, devices using Al and Cu foil as the contact layers exhibited a loading weight dependent output behavior, with the output increasing and then decreasing with increasing Cu NS loading (See Figure S6B,C, Supporting Information). In order to broaden the understanding of the counter material, the output of the HPC-TENG with a fixed Cu NS loading of 1.0 mg cm^{-2} was measured using insulating counter electrodes (i.e. film type: nylon and nitrile glove, fabric type: cotton and silk) positioned more favorably in the triboelectric series and compared with conductive counter electrodes. Interestingly, conductive counter electrodes consistently exhibited higher output than insulating counterparts, and this trend persisted even under high contact pressure of 158.3 kPa, as well as Cu thin-film TENG (see Figure S7, Supporting Information). We carefully estimate that this difference is attributed to the distinct contact configurations of metal–dielectric and dielectric–dielectric interfaces.[16] In SE-TENGs, insulating counter electrodes are limited by their lower saturation surface charge density and by localized trapped charges with poor redistribution capability,[54] which together reduce electrostatic induction efficiency compared to conductive electrodes. While further systematic studies are required to fully clarify this mechanism, these findings suggest that the electrical conductivity of the counter body can be considered as one of the factors governing the practical output of SE-TENGs. Additional measurements were conducted to evaluate the effect of operating parameters on output performance. Figure 3C,D present the output voltage of the HPC-TENG with a Cu NS loading weight of 1.0 mg cm^{-2} under varying vibration frequencies and applied pressures. The output voltage increased with increasing frequency from 1 to 5 Hz and with increasing pressure from 0.98 to 4.99 kPa. In addition to frequency and pressure, the effect of external load resistance on power output was also investigated. As shown in Figure 3E,F, the voltage, current density, and power density varied with external resistance, reaching a maximum power density of 260.4 μW cm^{-2} at 10 MΩ under a pressure of 83.3 kPa and a frequency of 2 Hz. To understand the origin of the significantly enhanced electrical output observed in the HPC-TENG, we conducted a comprehensive mechanistic analysis focusing on the device's internal architecture. While surface engineering and dielectric thickness are commonly known to affect TENG performance,[24] the unique hierarchical porous structure of the Cu NS film suggests that internal structure modulation may play a more dominant role in this case. Therefore, we first investigated the influence of the Cu NS-based electrode morphology on the charge induction mechanism. Subsequently, during the fabrication of the HPC-TENG, we examined whether the internal structure of the Cu NS film induced any changes in the PDMS surface morphology after spin-coating. **Figure 4A** schematically illustrates the charge induction mechanism of the HPC-TENG, which is fundamentally enhanced by its hierarchical porous structure. In conventional TENGs, the dielectric layer acts as a single capacitor, where triboelectric charges generated on the dielectric surface induce opposite charges on a planar electrode.[18] However, the hierarchical porous Cu NS film in the HPC-TENG forms a 3D network composed of stacked nanosheets with embedded voids. Upon infiltration with PDMS, these voids are filled to create multiple Cu NS–PDMS–Cu NS junctions, which act as microscale parallel capacitors within the dielectric layer. This intrinsic multi-capacitor configuration significantly increases the effective interfacial area for electrostatic induction, resulting in higher output voltage and current compared to planar electrodes. Figure 4B presents a comprehensive analysis of the relationship between the Cu NS loading weight, film thickness, and the corresponding power density of the HPC-TENG. The data reveal a non-linear dependence: as the Cu NS loading weight increases from 0.25 to 1.0 mg cm^{-2}, both the film thickness and power density sharply rise, indicating the formation of an optimal internal micro-capacitor architecture. At 1.0 mg cm^{-2}, the film reaches a critical structural configuration that enables the highest charge induction efficiency and maximum power density (≈174 μW cm^{-2}). However, further increases in loading (e.g., 2.0 and 4.0 mg cm^{-2}) result in a decline in power density despite thicker films. This performance degradation is attributed to the over- accumulation of conductive pathways within the Cu NS network, which can increase leakage currents and diminish the dielectric strength of the PDMS matrix, thereby disrupting efficient charge separation. For a deeper evaluation of the role of dielectric thickness, we systematically adjusted the Cu NS film and PDMS thicknesses. The results revealed that the output voltage reached a maximum when the infiltrated fraction was ≈2.1%, indicating that an optimal Cu NS–PDMS configuration is required to balance enhanced charge induction with minimized leakage (Figure S8, Supporting Information).

To further elucidate the mechanism responsible for the performance enhancement of the HPC-TENG, electrostatic simulations (COMSOL Multiphysics, Electrostatics) were conducted by comparing a planar PDMS/Cu thin-film electrode with the PDMS-HPC electrode, in which Cu loading was modeled by stacked nanosheet arrays embedded within PDMS (Figure S9, Supporting Information). In the planar configuration, charge induction occurs only across a single dielectric–metal interface, leading to limited capacitance and relatively low induced potential. In contrast, the HPC electrode exhibits a more negative induced potential than the planar system, and the potential becomes progressively stronger with increasing Cu-NS loading (Figure 4C,D). These results indicate that triboelectric charges at the PDMS surface not only induce charges at the external electrode but also couple with the internal Cu/PDMS interfaces. This coupling gives rise to interfacial polarization, akin to Maxwell–Wagner–Sillars polarization in multi-layered dielectrics, which introduces additional internal electric fields within the composite. The hierarchical porous network thereby acts as an array of Cu–PDMS–Cu micro-capacitors, expanding the effective interfacial area for charge induction, redistributing the internal electric field, and enhancing dielectric polarization, thereby increasing capacitance and charge induction efficiency.[55–58]

To further substantiate the simulation results and gain deeper insight into the underlying mechanism, we experimentally investigated the dielectric properties of the HPC-TENG. Dielectric property measurements provide experimental validation of this

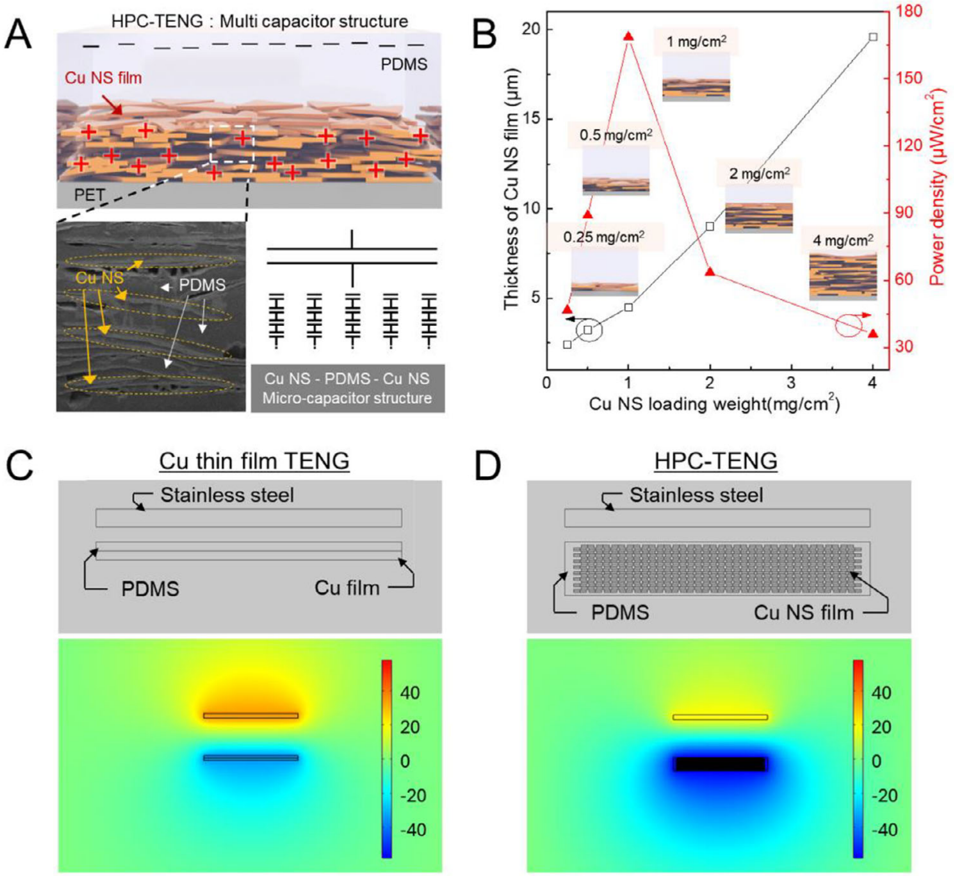

Figure 4. A) Schematic illustration of the charge induction mechanism in the HPC-TENG, highlighting the enhanced capacitance enabled by the hierarchical porous structure composed of numerous embedded microcapacitors formed by Cu NS–PDMS–Cu NS configurations. The "–" symbols represent surface charges generated by contact electrification, while the "+" symbols indicate the induced charges resulting from electrostatic induction. B) Thickness of the Cu NS film and corresponding power density of the HPC-TENG as a function of Cu NS loading weight. C) Simulation of the Surface electric potential distribution of Cu thin-film TENG and D) HPC-TENG.

mechanism (Figure S10, Supporting Information). As shown in Figure S10A,B (Supporting Information), the capacitance (and dielectric constant) of the HPC layer increases with Cu NS loading, reaching a maximum (≈18–19 pF) at ≈1.0 mg cm^{-2}, which is significantly higher than that of the Cu thin-film control (≈12 pF). This enhancement directly reflects the contribution of the distributed micro-capacitor network, which amplifies interfacial polarization and supports more efficient charge induction. In contrast, the loss tangent value increases with loading weight, reaching its highest value at 4.0 mg cm^{-2} (Figure S10C, Supporting Information). These results support that the PDMS structure infiltrated into the hierarchical porous Cu NS film enhances the capacitance of the HPC-TENG, while excessive loading weight leads to substantial charge loss, thereby causing a decline in output performance. The trends in capacitance and loss tangent with respect to Cu NS loading are well consistent with the output behavior of the TENG (Figure S10D, Supporting Information). Given these observations, it is important to investigate how structural factors contribute to the rise in loss tangent at higher loading conditions (2.0 and 4.0 mg cm^{-2}). In particular, nanosheet aggregation and related morphological effects are likely to play a central role. We examined the surface roughness of the Cu NS films as a function of loading weight using SEM and a 3D optical profiler (Figure S11, Supporting Information). The results revealed that excessive Cu NS loading leads to greater aggregation of nanosheets during the spray-coating process. This roughened surface leads to locally thinner PDMS regions at the peaks of the aggregated nanosheets. These regions serve as leakage pathways, which increase the leakage current and reduce the overall output. In addition to this morphological roughening, another factor that can lower the performance of TENGs at high Cu NS loading is the internal electric field screening effect, which arises from the increased fraction of metallic fillers within the Cu NS–PDMS composite.[58,59] This screening reduces the effective induction field inside the dielectric and further limits the achievable output.

To isolate the effect of internal structure from surface characteristics, we compared the PDMS surface morphology across all devices using SEM (See Figure S12, Supporting Information). All samples, regardless of Cu NS loading or electrode type, exhibited similar surface textures, indicating that surface roughness did not significantly influence the output. These findings collectively confirm that the enhanced performance of the HPC-TENG originates primarily from the internal architecture of the hierarchical

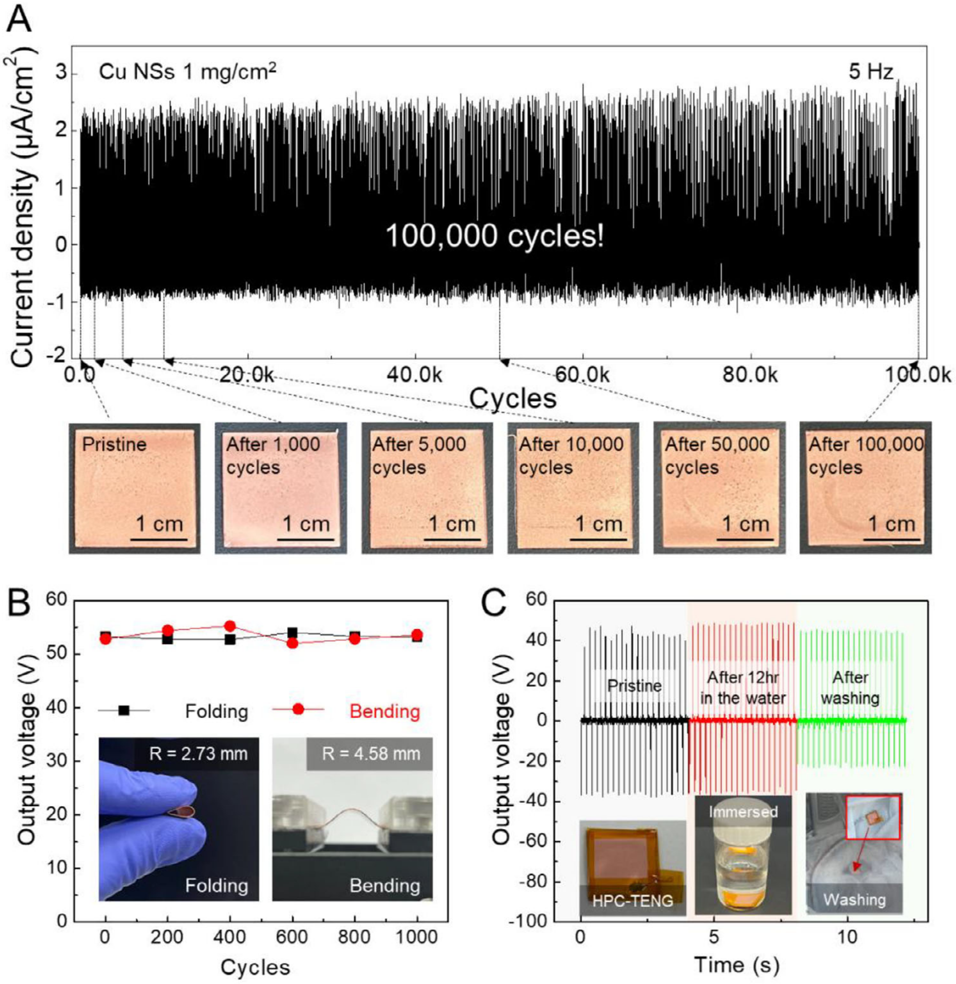

Figure 5. Stability and durability tests of the HPC-TENG. A) Output current density during 100 000 contact–separation cycles at 5 Hz (≈5.56 h), with surface images of the device at pristine, 1, 5, 10, 50, and 100k cycles. B) Output voltages after 1 000 folding and 1 000 bending cycles. C) Output voltages of the device after immersion in water for 12 h and after machine washing, demonstrating stable performance for wearable applications.

porous Cu NS network, which enables efficient embedded micro-capacitor formation, maximized charge-induction area, and scalable energy conversion. Building on the confirmation that the enhanced performance originates from the internal hierarchical porous structure, we next examined whether this architecture also affects the electrostatic behavior of the device, particularly its ability to retain surface potential (Figure S13, Supporting Information). The amount of potential decay was similar regardless of the Cu NS loading. Previous studies have reported that dip-trapped charges enhance surface potential retention, thereby improving TENG performance.[60,61] The comparable potential decay observed in both Cu thin-film TENGs and HPC-TENGs indicates that the performance enhancement of HPC-TENGs arises not from increased retention due to dip-trapped charges, but from internal polarization and enhanced charge induction efficiency.

Beyond achieving high output performance, ensuring long-term stability under continuous contact–separation cycles is essential for wearable applications.[15] Moreover, to account for practical usage conditions such as humid environments and mechanical deformations, we conducted a series of tests to verify the durability, structural stability, and environmental resistance of the HPC-TENG. The durability of the HPC-TENG was evaluated over 100 000 operating cycles (≈5.56 h at 5 Hz), during which no significant degradation in current density was observed, and no major deformation of the device occurred, except for slight PDMS delamination at the surface after 50 000 cycles (**Figure 5A**). Cross-sectional analysis of pristine samples and those after 1 000, 5 000, 10 000, 50 000, and 100 000 cycles confirmed that the internal PDMS-infiltrated structure remained intact without collapse (Figure S14, Supporting Information), supporting the stable output performance observed over 100 000 cycles. The mechanical robustness of the device was confirmed as it retained stable output after 1,000 folding and bending cycles (Figure 5B). Reliable performance was also maintained after 12 h of water immersion and machine washing (Figure 5C; Figure S15, Supporting Information), demonstrating excellent water resistance and washability.

In addition, to demonstrate the scalability and simplicity of the fabrication process, a Cu NS film was spray-coated on a 10 cm ×

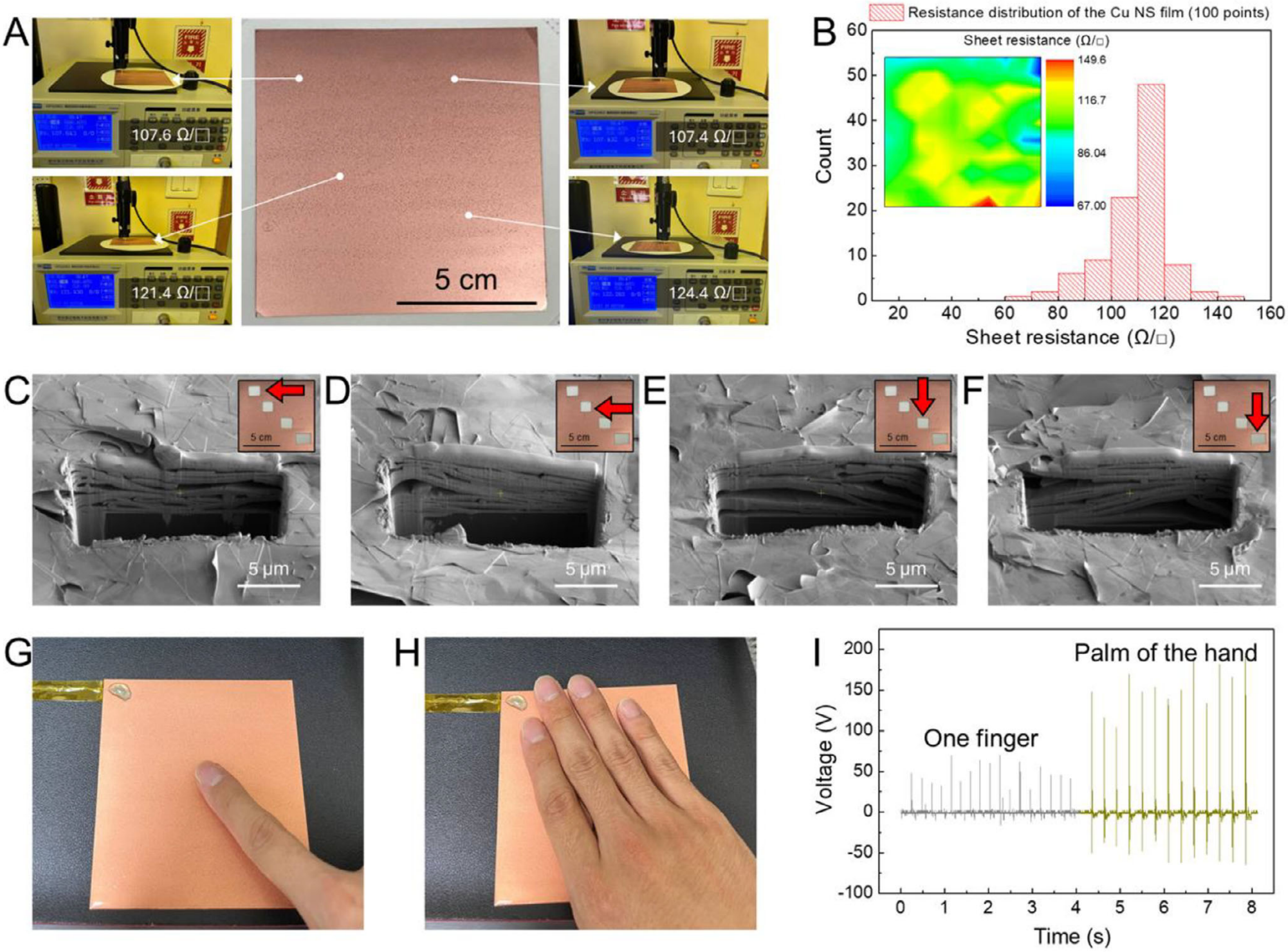

Figure 6. A) Photograph showing the sheet resistance measurement at different regions of the large-area HPC-TENG. B) Distribution map of sheet resistance across 100 measurement points on the large-area HPC-TENG. C–F) Cross-sectional analysis of the large-area HPC-TENG at the corresponding regions. G) Photograph of the HPC-TENG being contacted by a finger. H) Photograph of the HPC-TENG being contacted by a palm of the hand. I) Output voltage comparison of the HPC-TENG during contact–separation with a finger and palm.

10 cm PET substrate under a loading weight of 1.0 mg cm^{-2}. The sheet resistance was measured at 100 points across the film to evaluate its uniformity, revealing only minor variations of a few tens of ohms per square over the entire area (**Figure** 6A,B). To further confirm this, four regions of the film were selected, and the thickness of each region was analyzed via cross-sectional SEM images, showing a uniform Cu NS film with an average thickness of 4.66 μm and a thickness variation of ≈0.5 μm (Figure 6C–F). Subsequently, a PDMS layer was coated on the large-area Cu NS film to fabricate the HPC-TENG, and the output voltage was measured using both a finger and a palm, resulting in peak output voltages of 70 and 191 V, respectively (Figure 6G–I).

The practical capability of the HPC-TENG was further validated by designing a circuit in which the alternating output signal was rectified and stored in a capacitor (**Figure** 7A). The charging process was monitored using a multimeter (Figure 7B), and under an operating frequency of 5 Hz and an applied pressure of 4.99 kPa, a 470 μF capacitor was charged to 1.5 V. The stored energy was then used to operate a temperature and humidity sensor requiring 1.5 V, which remained functional for more than 30 s (Figure 7C). A detailed demonstration of the capacitor charging process and the operation of these small electronic devices is provided in Videos S2–S4 (Supporting Information), demonstrating the potential of the HPC-TENG for powering practical portable and wearable systems. In addition, the stored charge was sufficient to light up an LED (Figure 7D).

In addition to energy harvesting, the unique structural and electrical characteristics of the Cu NS film also enable its application in EMI shielding and Joule heating. The hierarchical porous architecture and the interconnected 2D nanosheet network not only facilitate effective attenuation of electromagnetic waves but also allow efficient heat generation under applied voltage. To evaluate the EMI shielding effectiveness of the HPC-TENG, a sample with dimensions of 2 cm × 3 cm was fabricated in accordance with the measurement equipment specifications. Using a network analyzer, the EMI shielding performance was measured in the X-band frequency range (8.2 to 12.4 GHz).

Figure 8A presents a schematic illustration of the EMI shielding measurement setup, while Figure 8B shows the schematic of the proposed EMI shielding mechanism of the HPC-TENG.

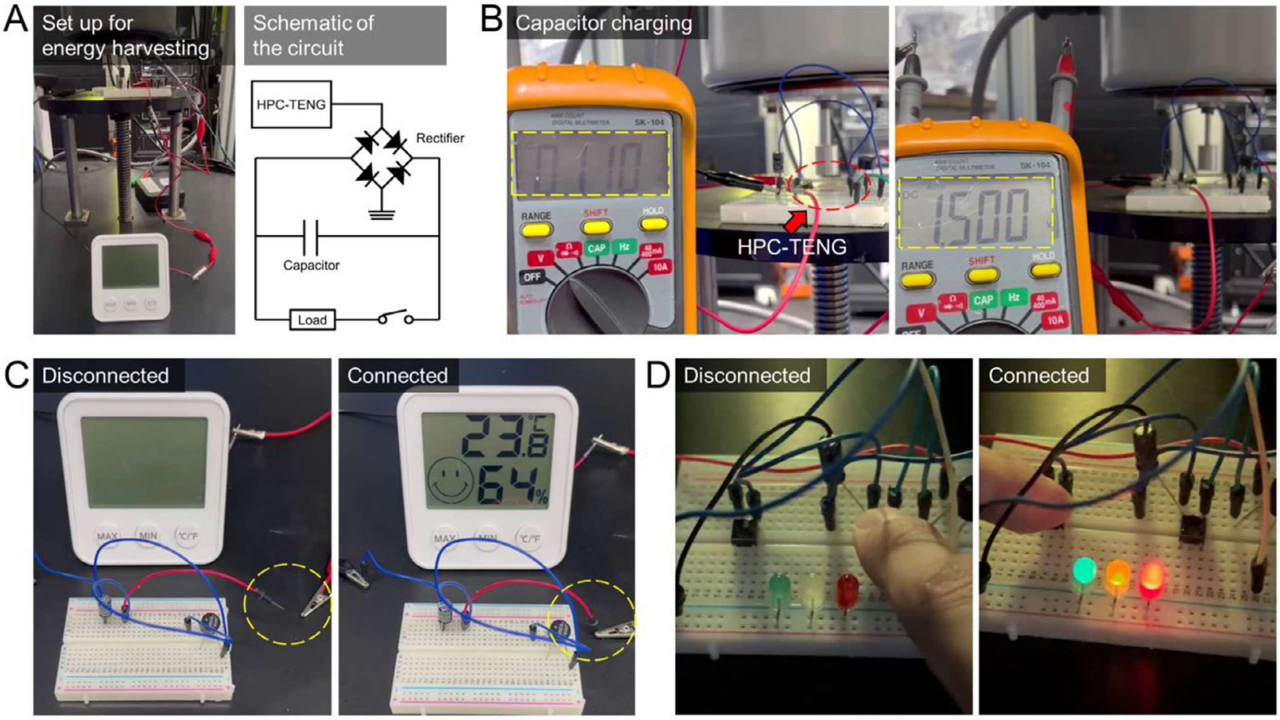

Figure 7. Powering electronic devices using the HPC-TENG. A) Schematic diagram and experimental setup for energy harvesting. B) Photograph showing capacitor charging by the HPC-TENG, where the increasing voltage is monitored with a multimeter connected across the capacitor. C) Photograph of a temperature and humidity sensor powered by the capacitor charged with the HPC-TENG. D) Photograph of an LED illuminated by the capacitor charged with the HPC-TENG.

The porous Cu NS film exhibits excellent EMI shielding performance mainly due to its hierarchical internal structure, which induces multiple internal reflections and absorption of electromagnetic waves through scattering between nanosheets, rather than surface reflection.[49] As shown in Figure 8C, the EMI shielding effectiveness of the HPC-TENG increases with the Cu NS loading weight, suggesting that the development of the internal porous structure contributes to enhanced shielding. A more detailed analysis separating absorption and reflection contributions is provided in Figure S16 (Supporting Information). This analysis clearly demonstrates that the absorption contribution significantly increases with nanosheet loading weight, while the reflection contribution remains nearly constant, unambiguously confirming that absorption, driven by the porous network, is the dominant and tunable mechanism responsible for the enhanced EMI shielding performance. After 5,000 contact-separation cycles, the EMI shielding performance was re-measured, as depicted in Figure 8D. Only a slight reduction in shielding effectiveness was observed, suggesting that the HPC-TENG maintains its EMI shielding performance even after repeated mechanical operation.

To evaluate the Joule heating capability of the HPC-TENG, we applied a direct current (DC) voltage and monitored the real-time thermal response using an infrared (IR) camera. As shown in **Figure 9A**, a series of thermal images illustrate the steady-state surface temperature of HPC-TENG devices with varying Cu nanosheet (NS) loading weights under an applied voltage of 5.0 V for 15 min. The device with the lowest loading weight (0.25 mg cm^{-2}) exhibited a modest temperature rise to 28.5 °C, while increasing the Cu NS content to 4.0 mg cm^{-2}resulted in a substantial temperature elevation to 59.4°C. This strong correlation between loading weight and heating performance clearly confirms that the heat generation is predominantly governed by the electrical conductivity of the Cu NS film.

The underlying mechanism is further clarified by the contour map in Figure 9B, which visualizes the temporal and thermal evolution of HPC-TENGs with different Cu NS loadings over a 30-min period at 5.0 V. Devices with higher loading weights not only achieved higher equilibrium temperatures but also exhibited faster heating rates. This behavior is attributed to the reduced sheet resistance of the Cu NS films at higher loading weights, which allows greater current flow under constant voltage, thereby increasing Joule heating efficiency as described by Joule's law.[62] To further validate the tunability of thermal output, we conducted additional measurements under both 3.0 V and 5.0 V conditions, with results presented in Figures S17 and S18 and Tables S2 and S3 (Supporting Information). These comprehensive datasets reveal a clear, reproducible trend: temperature rise scales with both applied voltage and Cu NS loading weight, offering a robust method for tailoring heating performance. Beyond verifying individual functions, the critical test is whether the HPC-TENG can sustain stable operation of its thermal and EMI shielding capabilities at the same time, as would be necessary for integrated wearable applications. To validate this multifunctional capability simultaneously, we fabricated a 2 cm × 8 cm HPC-TENG

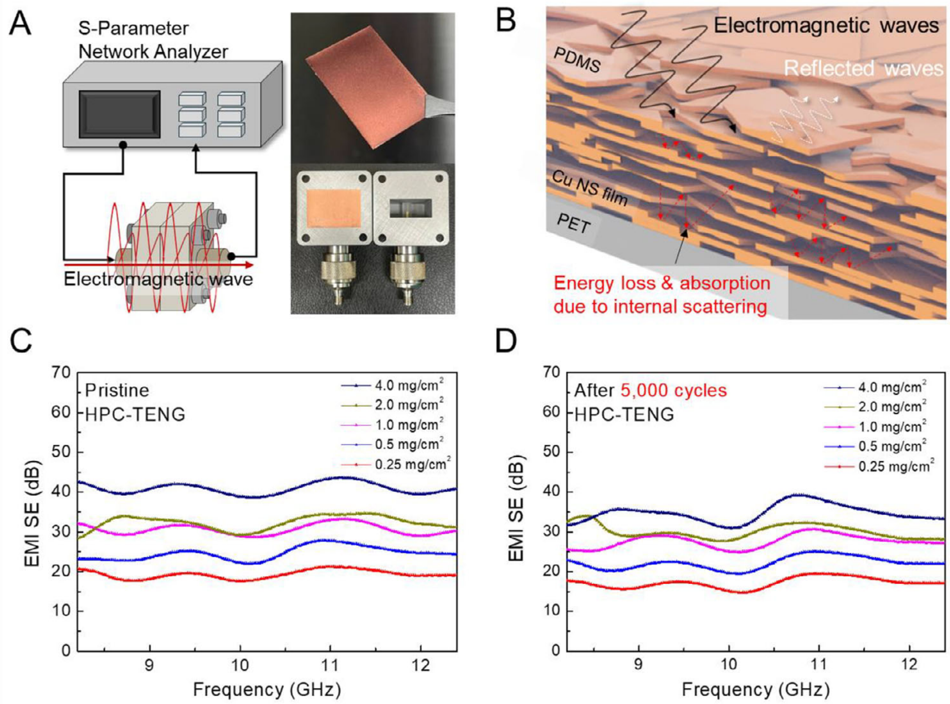

Figure 8. EMI shielding effectiveness (SE) and mechanical stability of HPC-TENG devices. A) Photograph and schematic illustration of the experimental setup for measuring EMI SE. B) Schematic diagram illustrating electromagnetic wave reflection, absorption, and internal scattering within the HPC-TENG device. C) EMI SE performance of pristine HPC-TENGs with varying Cu nanosheet loading weights (0.25–4.0 mg cm^{-2}). D) EMI SE performance after mechanical cycling (5,000 contact–separation cycles), demonstrating sustained stability.

device (1.0 mg cm^{-2} Cu NS loading) and applied a DC bias of 1.0 – 5.0 V across the Cu NS electrode while concurrently evaluating both its heating behavior and EMI shielding effectiveness (Figure S19A–C, Supporting Information). The infrared thermal images revealed a controllable temperature rise from ≈25.7 °C under pristine conditions to 41.1 °C at 5.0 V, while the EMI shielding performance remained stable and nearly unchanged across the entire voltage range. This result demonstrates that the HPC-TENG can simultaneously deliver Joule heating and EMI shielding without any compromise in performance, highlighting its robustness and reliability under realistic operating conditions. Moreover, the ability to modulate surface temperature simply by

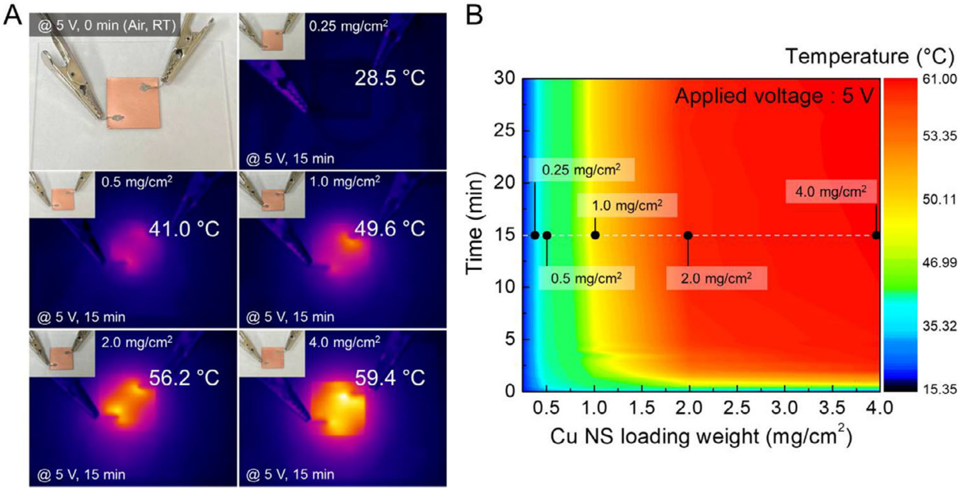

Figure 9. Application of the HPC-TENG as a flexible heater. A) Photograph and thermal infrared (IR) images illustrating surface temperature increase of HPC-TENG devices with varying Cu nanosheet loading weights (0.25–4.0 mg cm^{-2}) after applying 5 V for 15 min. B) Contour map depicting the surface temperature dependence on Cu nanosheet loading weight and heating duration at a constant voltage of 5.0 V.

adjusting the Cu NS film thickness or the applied voltage further expands its potential for next-generation multifunctional applications such as wearable thermal management, integrated EMI protection, and on-demand therapeutic heating platforms.

To comprehensively assess the multifunctional capabilities of the HPC-TENG, four key performance metrics were compared: peak output voltage, peak current density, average EMI shielding effectiveness (SE) in the X band, and surface temperature after 10 min under an applied voltage of 5.0 V, as a function of Cu NS loading weight (See Figure S20, Supporting Information) The results reveal a clear trade-off relationship between electrical output and other functionalities. Specifically, the output voltage and current density exhibit a distinct peak at a loading weight of 1.0 mg cm^{-2}, attributed to the optimal balance between charge induction efficiency and dielectric integrity. In contrast, both EMI shielding performance and Joule heating characteristics progressively improve with increasing loading weight, driven by enhanced electrical conductivity and thermal dissipation through the thicker Cu NS network. This multifunctionality suggests that fine-tuning the Cu NS loading not only maximizes the triboelectric output but also enables concurrent improvements in EMI shielding and thermal management. The hierarchical porous architecture of the Cu NS electrode plays a pivotal role in harmonizing these competing demands by offering an expanded interfacial area, efficient charge transport pathways, and embedded micro-capacitor networks. Building on these performance advantages, the electrical performance of the HPC-TENG was compared with previously reported single-electrode TENGs operating in vertical contact-separation mode. The HPC-TENG exhibited superior durability and competitive power density, while also providing additional multifunctional advantages such as EMI shielding and Joule heating, which collectively highlight its significance for practical applications (Figure S21 and Table S4, Supporting Information). Therefore, these findings underscore the material's capacity to serve as an integrative platform for next-generation multifunctional self-powered electronics.

3. Conclusion

In summary, we have demonstrated a structurally engineered hierarchical porous copper nanosheet (Cu NS) based single-electrode triboelectric nanogenerator (HPC-TENG) that significantly outperforms conventional Cu thin-film-based TENGs. Leveraging the spontaneous horizontal assembly of 2D single crystalline Cu NSs, our HPC-TENG achieves enhanced electrical output, exhibiting superior voltage and current densities alongside exceptional long-term stability over 100 000 contact-separation cycles. Crucially, this robust performance is attained solely through internal structural modification, employing a single dielectric and electrode material in a straightforward, scalable solution-based fabrication approach. Furthermore, the uniformity of large-area fabrication has also been validated, underscoring the practical scalability of the process. Beyond energy harvesting, the resulting HPC-TENG platform delivers multifunctional capabilities, including durable electromagnetic interference (EMI) shielding effectiveness exceeding 30 dB even after 5 000 operational cycles, and highly efficient, tunable Joule heating, reaching temperatures up to 59.4 °C at an applied voltage of only 5.0 V. These combined functionalities, arising intrinsically from the hierarchical porous architecture and solution-infiltrated electrode structure, position the HPC-TENG as a powerful and versatile energy harvesting and multifunctional electronic system. Our findings thus pave the way for practical integration into next-generation wearable electronics, flexible heating modules, EMI shielding materials, and self-powered systems.

4. Experimental Section

Materials: Copper(II) chloride dihydrate ($CuCl_2 \cdot 2H_2O$, ≥99.0%), D-(+)-glucose (≥99.5%), hexadecylamine (HDA, 98%), and iodine (I_2, ≥99.8%) were obtained from Sigma-Aldrich. Chloroform (CF, 99.5%), isopropyl alcohol (IPA, 99.5%), and acetone (AC, 99.5%) were supplied by Samchun Pure Chemical Industry Co., Ltd. Polydimethylsiloxane (PDMS) and its curing agent (Sylgard 184 A & B) were purchased from Dow Corning. PET substrates with dimensions of 2 cm × 2 cm and 2 cm × 3 cm were used. Five nines copper pellets (3 mm × 3 mm) were obtained from Itasco (South Korea). ELCOAT silver resin paste was purchased from CANS (Japan).

Preparation of Cu Nanosheets: A hydrothermal approach was employed to synthesize 2D single-crystalline copper nanosheets. Iodine (I_2, 0.0313 mg mL^{-1}) was dissolved in deionized water by stirring at 75 °C and 1300 rpm until fully dissolved. This iodide-containing solution was then combined with copper(II) chloride dihydrate ($CuCl_2 \cdot 2H_2O$, 6.3 mg mL^{-1}), D-(+)-glucose (7.3 mg mL^{-1}), and hexadecylamine (HDA, 43.7 mg mL^{-1}) in deionized water at room temperature. The resulting mixture was transferred to an autoclave and reacted in a convection oven at 100 °C for 12 h. Following the reaction, the copper nanosheets were isolated through multiple centrifugation cycles using hot deionized water and chloroform to ensure thorough purification. The purified Cu NSs were placed onto a Si/SiO_2 substrate, and their crystallographic orientation was analyzed by electron backscatter diffraction (EBSD) using a field-emission scanning electron microscope (FE-SEM, HITACHI SU70).

Fabrication of HPC-TENG: The HPC-TENG consisted of a substrate, electrode, and dielectric layer, which were PET, Cu NS film, and PDMS, respectively. To fabricate Cu NS films, the synthesized and purified Cu NSs were dispersed in chloroform and spray-coated onto 2 cm × 2 cm PET substrates using a commercially available hand-held airbrush (Harder & Steenbeck). The PET substrate was cleaned using acetone and IPA. To investigate the effect of Cu NS loading weight, Cu NS films with target loading weights of ≈0.25, 0.5, 1.0, 2.0, and 4.0 mg cm^{-2} were prepared. The Cu NS films were dried on a hot plate at 70 °C for 5 min. PDMS was prepared by mixing the elastomer and curing agent at a 10:1 ratio, followed by vacuum treatment for 30 min to remove trapped air bubbles. Subsequently, the PDMS mixture was spin-coated onto the prepared Cu NS film at 500 rpm for 60 s and then cured in a convection oven at 80 °C for 2 h. For comparison, a 100 nm-thick Cu thin-film was deposited onto a PET substrate at a deposition rate of 1.0 Å s^{-1} using a thermal evaporator (JV21EVA-F30k2p, JVAC) under a pressure of 2×10^{-7} Torr. PDMS was then spin-coated and cured on top of the Cu thin-film using the same procedure described above. For the electrical characterization of the fabricated HPC-TENG, the Cu NS film was connected to external wires using silver paste (ELCOAT P-100, CANS).

Characterization and Device Demonstrations of HPC-TENG: For EMI shielding effectiveness (EMI SE) measurements, the HPC-TENG was fabricated on a 2 cm × 3 cm PET substrate according to the instrument specifications, using the same procedure described above. The sheet resistance of the Cu NS film was measured using a four-point probe system (HPS 2663, HELPASS). The 3D structural analysis was carried out using a 3D X-ray Tomography Microscope System (Xradia Ultra, Zeiss). Surface and cross-sectional analyses of the Cu NS film were conducted by field-emission scanning electron microscopy (Gemini500, Carl Zeiss) installed in the Center for University-wide Research Facilities (CURF) at Jeonbuk National University, after milling with a focused ion beam system at SPRC (Helios 5 CX, Thermo Fisher Scientific, NFEC-2023-01-284927). In addition, the surface topography of the Cu NS film was characterized using a 3D profiler (3D Profilm, Filmetrics). Similarly, the cross-section of the HPC-TENG after PDMS coating was also prepared using the same FIB milling method and analyzed by FE-SEM. For the electrical characterization of the HPC-TENG, an oscilloscope (DSO5202P, Hantek) and an electrometer (KEITHLEY 6514) were used. One channel of each instrument was connected to the HPC-TENG, while the other was grounded. To apply periodic pressure at a constant frequency during measurements, a waveform generator (Agilent 33220A) and a power amplifier (PA-138) were employed. The dielectric properties of PDMS were measured using a LCR meter (Wayne Kerr 4100) in the frequency range of 20–100 000 Hz. The surface potential of the HPC-TENG was measured using an Electrostatic Fieldmeter (FMX-004). The mechanical durability of HPC-TENG was evaluated through a mechanical bending test, employing a step motor controller (SMC-100, ECOPIA). The EMI SE was measured in the X-band frequency range (8.2–12.4 GHz) using an S-parameter network analyzer (Agilent 8720ES). The heating behavior of the HPC-TENG was assessed by applying DC voltages of 3.0 and 5.0 V for 30 min using a KEYSIGHT 33500B waveform generator. Temperature changes during this process were tracked using a Testo 875 thermal imager (Testo 875i basic, Germany). For the demonstration of energy harvesting using the HPC-TENG, a breadboard, bridge rectifier (W06M), 470 µF capacitor (10.0 V, 85 °C), breadboard-friendly 4-pin switch (SZHTH0018), and 5 mm LEDs (red, yellow, green) were used.

Electrostatic Simulation of HPC-TENG: To clarify the proposed electricity-generation mechanism, electrostatic potential distributions were simulated using COMSOL Multiphysics (AC/DC module, Electrostatics) with a simplified 2D geometry. The upper electrode (stainless steel) and a strip-array Cu lower electrode encapsulated in PDMS were modeled according to the device structure. The Cu loading was controlled by varying the number of stacked strip layers ($L = 4$–16). Triboelectric charges were introduced as fixed surface-charge densities on the frictional interfaces, and a small charge density was also applied at the Cu–PDMS interface to account for internal charge transfer. The metal boundaries were set as floating potentials grouped by electrode, while the air domain boundary was grounded. Stationary solutions were obtained, and the potential of the lower electrode was extracted as line-averaged values.

Supporting Information

Supporting Information is available from the Wiley Online Library or from the author.

Acknowledgements

This work was supported by the National Research Foundation of Korea (RS-2024-00452255, RS-2024-00406152) and the Commercialization Promotion Agency for R&D Outcomes (COMPA) grant funded by the Korean Government (Ministry of Science and ICT) (RS-2023-00304743)

Conflict of Interest

The authors declare no conflict of interest.

Data Availability Statement

The data that support the findings of this study are available from the corresponding author upon reasonable request.

Keywords

2D copper nanosheets, hierarchical porous structure, HPC-TENG, self-powered system, solution-infiltrated structure, triboelectric nanogenerator

Received: August 9, 2025
Revised: September 29, 2025
Published online: October 21, 2025

---

[1] Z. L. Wang, *Mater. Today.* **2017**, *20*, 74.
[2] Z. L. Wang, *ACS Nano* **2013**, *7*, 9533.
[3] S. Hwang, M. Kang, A. Lee, S. Bae, S.-K. Lee, S. H. Lee, T. Lee, G. Wang, T.-W. Kim, *Nat. Commun.* **2022**, *13*, 3173.
[4] J. A. Rogers, T. Someya, Y. Huang, *Science* **2010**, *327*, 1603.
[5] L. Hu, P. L. Chee, S. Sugiarto, Y. Yu, C. Shi, R. Yan, Z. Yao, X. Shi, J. Zhi, D. Kai, H.-D. Yu, W. Huang, *Adv. Mater.* **2023**, *35*, 2205326.
[6] D. Corzo, G. Tostado-Blázquez, D. Baran, *Front. Electron.* **2020**, *1*, 594003.
[7] X. Chen, D.-H. Kim, N. Lu, *Chem. Rev.* **2024**, *124*, 6145.
[8] C. Wang, K. Xia, H. Wang, X. Liang, Z. Yin, Y. Zhang, *Adv. Mater.* **2019**, *31*, 1801072.
[9] Y.-W. Chong, W. Ismail, K. Ko, C.-Y. Lee, *IEEE Sens. J.* **2019**, *19*, 9047.
[10] M. A. Hanson, H. C. Powell Jr., A. T. Barth, K. Ringgenberg, B. H. Calhoun, J. H. Aylor, *Computer* **2009**, *42*, 58.
[11] Z. L. Wang, *Faraday Discuss.* **2014**, *176*, 447.
[12] S. Priya, D. J. Inman, *Energy Harvesting Technologies*, Springer, New York, **2009**.
[13] A. Khaligh, O. C. Onar, *Energy Harvesting: Solar, Wind, and Ocean Energy Conversion Systems*, CRC Press, Boca Raton, **2010**.
[14] M. Cai, Z. Yang, J. Cao, W.-H. Liao, *Energy Technol.* **2020**, *8*, 2000533.
[15] R. D. I. G. Dharmasena, S. R. P. Silva, *Nano Energy* **2019**, *62*, 530.
[16] Z. L. Wang, A. C. Wang, *Mater. Today* **2019**, *30*, 34.
[17] S. Niu, Z. L. Wang, *Nano Energy* **2015**, *14*, 161.
[18] W. Akram, Q. Chen, G. Xia, J. Fang, *Nano Energy* **2023**, *106*, 108043.
[19] L. Zhou, D. Liu, J. Wang, Z. L. Wang, *Friction* **2020**, *8*, 481.
[20] C. Ning, L. Tian, X. Zhao, S. Xiang, Y. Tang, E. Liang, Y. Mao, *J. Mater. Chem. A.* **2018**, *6*, 19143.
[21] T. An, D. V. Anaya, S. Gong, L. W. Yap, F. Lin, R. Wang, M. R. Yuce, W. Cheng, *Nano Energy* **2020**, *77*, 105295.
[22] Q. Shi, Z. Zhang, T. Chen, C. Lee, *Nano Energy* **2019**, *62*, 355.
[23] Q. Shi, C. Lee, *Adv. Sci.* **2019**, *6*, 1900617.
[24] F.-R. Fan, L. Lin, G. Zhu, W. Wu, R. Zhang, Z. L. Wang, *Nano Lett.* **2012**, *12*, 3109.
[25] J. He, Z. Xie, K. Yao, D. Li, Y. Liu, Z. Gao, W. Lu, L. Chang, X. Yu, *Nano Energy* **2021**, *81*, 105590.
[26] C. Wu, A. C. Wang, W. Ding, H. Guo, Z. L. Wang, *Adv. Energy Mater.* **2019**, *9*, 1802906.
[27] A. Babu, S. Gupta, R. Katru, N. Madathil, A. Kulandaivel, P. Kodali, H. Divi, H. Borkar, U. K. Khanapuram, R. K. Rajaboina, *Energy Technol.* **2024**, *12*, 2400796.
[28] A. Babu, K. Ruthvik, P. Supraja, M. Navaneeth, K. U. Kumar, R. R. Kumar, K. Prakash, N. Raju, *J. Mater. Sci.: Mater. Electron.* **2023**, *34*, 2195.
[29] A. Babu, N. Madathil, R. K. Rajaboina, H. Borkar, K. C. Devarayapalli, Y. K. Mishra, S. Hajra, H. J. Kim, U. K. Khanapuram, D. S. Lee, *Mater. Adv.* **2025**, *6*, 4725.
[30] L. Bochu, A. Babu, S. Potu, U. K. Khanapuram, R. K. Rajaboina, P. Kodali, *ACS Appl. Polym. Mater.* **2025**, *7*, 4132.
[31] R. Kruchinin, Y. Nurmakanov, G. Nauryzbayev, D. Adair, Z. Bakenov, G. Kalimuldina, *Energy Rep.* **2022**, *8*, 15048.
[32] A. Haleem, Z. Haider, R. u. S. Ahmad, U. P. Claver, A. Shah, G. Zhao, W.-D. He, *Int. J. Energy Res.* **2022**, *44*, 8442.
[33] J. Chun, J. W. Kim, W.-S. Jung, C.-Y. Kang, S.-W. Kim, Z. L. Wang, J. M. Baik, *Energy Environ. Sci.* **2015**, *8*, 3006.
[34] L. Cheng, Y. Xi, C. Hu, X. Yue, G. Wang, *Energy Harvest. Syst.* **2016**, *3*, 91.
[35] C. Wu, T. W. Kim, J. H. Park, H. An, J. Shao, X. Chen, Z. L. Wang, *ACS Nano* **2017**, *11*, 8356.
[36] W. He, M. Sohn, R. Ma, D. J. Kang, *Nano Energy* **2020**, *78*, 105383.
[37] X. Xia, J. Chen, G. Liu, M. S. Javed, X. Wang, C. Hu, *Carbon* **2017**, *111*, 569.

[38] S. Nuthalapati, A. Chakraborthy, I. Arief, K. K. Meena, K. R. Kaja, R. R. Kumar, K. U. Kumar, A. Das, M. E. Altinsoy, A. Nag, *IEEE J. Flex. Electron.* **2024**, *3*, 393.
[39] N. Madathil, A. Babu, M. Velupula, A. Kulandaivel, R. K. Rajaboina, U. K. Khanapuram, K. C. Devarayapalli, D. S. Lee, *Sustainable Energy Fuels* **2025**, *9*, 4364.
[40] X. He, H. Guo, X. Yue, J. Gao, Y. Xi, C. Hu, *Nanoscale* **2015**, *7*, 1896.
[41] Z. Liu, M. Muhammad, L. Cheng, E. Xie, W. Han, *Appl. Phys. Lett.* **2020**, *117*, 143903.
[42] R. K. Rajaboina, U. K. Khanapuram, A. Kulandaivel, *Adv. Sensor Res.* **2024**, *3*, 2400045.
[43] J. Kim, H. Cho, M. Han, Y. Jung, S. S. Kwak, H.-J. Yoon, B. Park, H. Kim, J. Park, S.-W. Kim, *Adv. Energy Mater.* **2020**, *10*, 2002312.
[44] F. Shahzad, M. Alhabeb, C. B. Hatter, B. Anasori, S. M. Hong, C. M. Koo, Y. Gogotsi, *Science* **2016**, *353*, 1137.
[45] W.-T. Cao, F.-F. Chen, Y.-J. Zhu, Y.-G. Zhang, Y.-Y. Jiang, M.-G. Ma, F. Chen, *ACS Nano* **2018**, *12*, 4583.
[46] Y. Du, X. Wang, X. Dai, W. Lu, Y. Tang, J. Kong, *J. Mater. Sci. Technol.* **2022**, *100*, 1.
[47] P. Zhao, D. Gao, Y. Zhou, B. Lyu, J. Ma, *Chem. Eng. J.* **2025**, *522*, 167693.
[48] J.-W. Lee, J. Han, D. S. Lee, S. Bae, S. H. Lee, S.-K. Lee, B. J. Moon, C.-J. Choi, G. Wang, T.-W. Kim, *Small* **2018**, *14*, 1703312.
[49] H. K. Choi, A. Lee, M. Park, D. S. Lee, S. Bae, S.-K. Lee, S. H. Lee, T. Lee, T.-W. Kim, *ACS Nano* **2021**, *15*, 829.
[50] G. Pace, A. Ansaldo, M. Serri, S. Lauciello, F. Bonaccorso, *Nano Energy* **2020**, *76*, 104989.
[51] G. Zhu, Z.-H. Lin, Q. Jing, P. Bai, C. Pan, Y. Yang, Y. Zhou, Z. L. Wang, *Nano Lett.* **2013**, *13*, 847.
[52] Z. Wang, W. Liu, J. Hu, W. He, H. Yang, C. Ling, Y. Xi, X. Wang, A. Liu, C. Hu, *Nano Energy* **2020**, *69*, 104452.
[53] H. Zou, Y. Zhang, L. Guo, P. Wang, X. He, G. Dai, H. Zheng, C. Chen, A. C. Wang, C. Xu, Z. L. Wang, *Nat. Commun.* **2019**, *10*, 1427.
[54] Y. S. Zhou, S. Li, S. Niu, Z. L. Wang, *Nano Res.* **2016**, *9*, 3705.
[55] J. Zhong, X. Hou, J. He, F. Xue, Y. Yang, L. Chen, J. Yu, J. Mu, W. Geng, X. Chou, *Nano Energy* **2022**, *98*, 107289
[56] X. Xia, J. Chen, H. Guo, G. Liu, D. Wei, Y. Xi, X. Wang, C. Hu, *Nano Res.* **2017**, *10*, 320
[57] S. Niu, S. Wang, L. Lin, Y. Liu, Y. S. Zhou, Y. Hu, Z. L. Wang, *Energy Environ. Sci.* **2013**, *6*, 3576.
[58] B. Zhao, L. Lei, Y. Zhu, Z. Cheng, Y. Liu, S. Wang, M. Liu, T. Yu, W. Yang, Y. Li, *Chem. Eng. J.* **2023**, *461*, 142086.
[59] J. Mu, J. Song, X. Han, S. Xian, X. Hou, J. He, X. Chou, *Adv. Mater. Technol.* **2022**, *7*, 2101481.
[60] D. W. Kim, J. H. Lee, I. You, J. K. Kim, U. Jeong, *Nano Energy.* **2018**, *50*, 192.
[61] N. Cui, L. Gu, Y. Lei, J. Liu, Y. Qin, X. Ma, Y. Hao, Z. L. Wang, *ACS Nano* **2016**, *10*, 6131.
[62] J. Yuan, Y. Zhang, F. Chen, Z. Gu, *J. Mater. Chem. C.* **2024**, *12*, 14729.